The Astrophysical Journal, 980:68 (10pp), 2025 February 10 https://doi.org/10.3847/1538-4357/adabc8

Neutrino-dominated Relativistic Viscous Accretion Flows around Rotating Black Holes with Shocks

Amit Kumar, Sayan Chakrabarti, and Santabrata Das
Indian Institute of Technology Guwahati, Guwahati 781039, Assam, India; kamit@iitg.ac.in, sayan.chakrabarti@iitg.ac.in, sbdas@iitg.ac.in
Received 2024 November 4; revised 2025 January 1; accepted 2025 January 12; published 2025 February 5

Abstract

We investigate the relativistic, viscous, advective neutrino-dominated accretion flows (NDAFs) around rotating stellar-mass black holes, incorporating neutrino cooling. By adopting an effective potential to describe the spacetime geometry around the rotating black holes, we self-consistently solve the governing NDAF equations to obtain global transonic accretion solutions. Our findings indicate that, depending on the model parameters, namely, energy (ε), angular momentum (λ), accretion rate ($\dot{m}$), viscosity (α), and black hole spin ($a_{\rm k}$), NDAFs may harbor standing shocks where the Rankine–Hugoniot shock conditions are satisfied. Utilizing these shock-induced NDAF solutions, we compute the neutrino luminosity (L_{ν}) and neutrino annihilation luminosity ($L_{\nu\bar{\nu}}$) across a wide range of model parameters. We further calculate maximum neutrino luminosity ($L_{\nu}^{\rm max}$) and neutrino annihilation luminosity ($L_{\nu\bar{\nu}}^{\rm max}$), resulting in $L_{\nu}^{\rm max} \sim 10^{51-53}\,{\rm erg\,s^{-1}}$ ($10^{48-51}\,{\rm erg\,s^{-1}}$) and $L_{\nu\bar{\nu}}^{\rm max} \sim 10^{48-52}\,{\rm erg\,s^{-1}}$ ($10^{42-49}\,{\rm erg\,s^{-1}}$) for $a_{\rm k} = 0.99$ (0.0). These findings suggest that shocked NDAF solutions are potentially promising to explain the energy output of gamma-ray bursts (GRBs). We employ our NDAF model formalism to elucidate $L_{\nu\bar{\nu}}^{\rm obs}$ for five GRBs with known redshifts and estimate their accretion rate ($\dot{m}$) based on the spin ($a_{\rm k}$) of the central source of the GRBs studied here.

Unified Astronomy Thesaurus concepts: Accretion (14); Hydrodynamics (1963); Black hole physics (159); Shocks (2086)

1. Introduction

Gamma-ray bursts (GRBs) are among the most energetic events in the Universe, exhibiting an isotropic distribution across the sky (P. Mészáros 2001). They are also the most luminous explosions known, with luminosities reaching up to $10^{54}\,{\rm erg\,s^{-1}}$. Hence, the origins and underlying physical mechanisms of GRBs are the focus of extensive research.

In general, GRBs are classified based on their duration into two categories: short gamma-ray bursts (SGRBs), which last less than 2 s, and long gamma-ray bursts (LGRBs), which last more than 2 s (C. Kouveliotou et al. 1993). From the perspective of energy release, accretion onto black holes is considered an efficient mechanism (J. Frank et al. 2002). During accretion, matter revolves around a compact object like a black hole (BH) or a neutron star (NS) and converts its gravitational energy into radiation throughout the process. Indeed, the energy output of GRBs requires accretion rates on the order of a fraction of a solar mass per second up to several solar masses per second.

The probable progenitors of the SGRBs are thought to originate from the mergers of two NSs or a binary NS–BH system (D. Eichler et al. 1989; B. Paczynski 1991; R. Narayan et al. 1992), while LGRBs are mainly associated with the gravitational collapse of massive stars (S. E. Woosley 1993). These scenarios often result in a central compact object surrounded by a hyperaccretion disk, which is a plausible candidate for the central engine of GRBs. In such systems, the extremely high accretion rate causes the inner region of the hyperaccretion disk to become extremely dense ($\rho \sim 10^{8}-10^{12}\,{\rm g\,cm^{-3}}$) and hot ($T \sim 10^{10}-10^{11}\,{\rm K}$), rendering it optically thick ($\tau_{\gamma} \gg 1$). This opacity traps photons within the disk, preventing them from contributing to the high-energy emissions associated with GRBs. In contrast, a large number of energetic neutrinos can be emitted from the surface of the disk, which carries away the dissipated energy of the accreted matter. Eventually, the annihilation of neutrinos and antineutrinos can produce a relativistic electron–positron pair-dominated outflow, potentially powering a GRB. In the late nineties, R. Popham et al. (1999) first proposed the hyperaccreting neutrino-dominated accretion flow (NDAF) model and demonstrated that NDAFs around rotating stellar-mass black holes could serve as a viable central engine for GRBs. Since then, extensive efforts have been made in the literature to investigate different aspects of NDAF models in explaining GRB characteristics (R. Narayan et al. 2001; T. Di Matteo et al. 2002; K. Kohri & S. Mineshige 2002; S. Rosswog et al. 2003; K. Kohri et al. 2005; A. Janiuk et al. 2007; N. Kawanaka & S. Mineshige 2007; T. Liu et al. 2007, 2017; I. Zalamea & A. M. Beloborodov 2011; L. Xue et al. 2013; B.-G. Chen et al. 2022; Y.-F. Wei & T. Liu 2022). It is important to note that most of the aforementioned studies assume the flow to exhibit Keplerian motion during accretion, and the investigation of transonic behavior, including shocks in NDAFs, remains largely unexplored.

Motivated by this, in this work, we develop a formalism to study the steady, axisymmetric NDAF around rotating stellar-mass black holes. To account for gravitational effects, we utilize an effective potential that mimics the spacetime geometry surrounding the black hole. We adopt an equation of state that encompasses both gas and radiation pressure. Following S. K. Chakrabarti & S. Das (2004, and references therein), we adopt a mixed shear stress prescription to incorporate the effects of viscosity, which governs the transport

of angular momentum and heating of matter in NDAFs. Furthermore, the flow is cooled as it accretes toward the black hole, with neutrino cooling being the dominant radiative mechanism. Considering all this, we self-consistently solve the hydrodynamic equations that govern the dynamics of the neutrino-dominated accreting matter around stellar-mass rotating black hole and obtain global transonic solutions for a set of model parameters, such as energy (ε), angular momentum (λ), accretion rate ($\dot{m}$), viscosity (α) and black hole spin ($a_{\rm k}$). We find that during the course of accretion, NDAFs may undergo shock transitions where the Rankine–Hugoniot conditions (RHCs; L. D. Landau & E. M. Lifshitz 1959) are satisfied. Such shock-induced global solutions are examined both theoretically and numerically in various accretion environments around weakly ($a_{\rm k} \rightarrow 0$) as well as rapidly ($a_{\rm k} \rightarrow 1$) rotating black holes (J. Fukue 1987; S. K. Chakrabarti 1989; S. K. Chakrabarti & D. Molteni 1993; R. Yang & M. Kafatos 1995; D. Ryu et al. 1997; J.-F. Lu et al. 1999; P. A. Becker & D. Kazanas 2001; S. Das et al. 2001, 2009, 2014; S. K. Chakrabarti & S. Das 2004; S. Das 2007; T. Okuda & S. Das 2015; B. Sarkar & S. Das 2016; R. Aktar et al. 2017; P. Suková et al. 2017; I. K. Dihingia et al. 2018a, 2018b, 2019; B. Sarkar et al. 2018; T. Okuda et al. 2019; I. Palit et al. 2019; G. Sen et al. 2022; S. Mitra & S. Das 2024; S. Singh & S. Das 2024). We calculate the relevant flow variables and analyze their dependence on the accretion rate ($\dot{m}$). Furthermore, using the shocked NDAF solutions, we calculate the neutrino luminosity (L_{ν}) and neutrino annihilation luminosity ($L_{\nu\bar{\nu}}$), and examine how they vary with the model parameters. Finally, we discuss the astrophysical relevance of this work in explaining the GRB jet luminosities powered by the annihilation of neutrinos escaping from the disks.

This paper is organized as follows. In Section 2, we outline the model assumptions and describe the governing equations for studying NDAFs. In Section 3, we present the global NDAF solutions, both in the presence and absence of shocks. Section 4 discusses the astrophysical implications of our findings. Finally, in Section 5, we present concluding remarks.

2. Governing Equations

We consider steady, axisymmetric, relativistic, viscous, advective NDAFs around rotating stellar-mass black holes. Because of the asymmetry, we use a cylindrical coordinate system with the black hole located at the origin and choose $G = M_{\rm BH} = c = 1$, where G is the gravitational constant, $M_{\rm BH}$ is the mass of the black hole, and c refers to the speed of light. In this system, the radial coordinate, angular momentum, and energy of NDAF are expressed in units of $GM_{\rm BH}/c^2$, $GM_{\rm BH}/c$, and c^2, respectively.

Based on the above considerations, we formulate the following governing equations for NDAF, which are described below.

(1) Radial momentum equation:

$$v\frac{dv}{dx} + \frac{1}{\rho}\frac{dP}{dx} + \frac{d\Phi^{\rm eff}}{dx} = 0, \tag{1}$$

where x, v, and ρ are radial distance, radial velocity, and mass density of flow, respectively. The total pressure P of the flow is the sum of the gas pressure ($P_{\rm gas}$) and radiation pressure ($P_{\rm rad}$). The gas pressure is expressed as $P_{\rm gas} = \rho k_{\rm B} T/m_{\rm p}$, where $k_{\rm B}$, T, and $m_{\rm p}$ represent the Boltzmann constant, temperature of the flow, and mass of the ion. The radiation pressure is given by $P_{\rm rad} = 11\bar{a}T^4/12$. Here, $\bar{a}$ is the radiation constant and the factor $11/12$ accounts for the contribution of relativistic electron–positron pairs (T. Di Matteo et al. 2002). In Equation (1), $\Phi^{\rm eff}$ refers to effective potential that mimics the spacetime geometry around a rotating black hole (I. K. Dihingia et al. 2018a) and is given by

$$\Phi^{\rm eff} = \frac{1}{2}\ln\left[\frac{x\Delta}{a_{\rm k}^2(x+2) - 4a_{\rm k}\lambda + x^3 - \lambda^2(x-2)}\right], \tag{2}$$

where λ denotes the specific angular momentum of the flow, $a_{\rm k}$ is the spin of the black hole, and $\Delta = x^2 - 2x + a_{\rm k}^2$.

(2) Mass conservation equation:

$$\dot{M} = 2\pi v\Sigma\sqrt{\Delta}, \tag{3}$$

where $\dot{M}$ is the accretion rate which remains constant throughout the flow and Σ ($=2\rho H$) represents the vertically integrated mass density of flow (R. Matsumoto et al. 1984). The quantity H denotes the half thickness of the disk and is defined as (H. Riffert & H. Herold 1995; J. Peitz & S. Appl 1997)

$$H = \sqrt{\frac{Px^3}{\rho\mathcal{F}}}; \quad \mathcal{F} = \frac{1}{(1-\Omega\lambda)}\frac{(x^2+a_{\rm k}^2)^2 + 2\Delta a_{\rm k}^2}{(x^2+a_{\rm k}^2)^2 - 2\Delta a_{\rm k}^2},$$

where $\Omega \quad [=(2a_{\rm k} + \lambda(x-2))/(a_{\rm k}^2(x+2) - 2a_{\rm k}\lambda + x^3)]$ is the angular velocity of flow. In this work, we write $\dot{M}$ in units of solar mass per second and is expressed as $\dot{m} = \dot{M}/(M_{\odot} \quad {\rm s}^{-1})$.

(3) Azimuthal momentum equation:

$$\Sigma v x\frac{d\lambda}{dx} + \frac{d}{dx}(x^2 W_{x\phi}) = 0, \tag{4}$$

where $W_{x\phi}[= -\alpha(W + \Sigma v^2)]$ is the $x\phi$ component of the viscous stress (S. K. Chakrabarti & D. Molteni 1995), W ($=2PH$) is the vertically integrated pressure and α is the viscosity parameter.

(4) Entropy generation equation:

$$\Sigma v T\frac{ds}{dx} = \Sigma v\left(\frac{du}{dx} - \frac{P}{\rho^2}\frac{d\rho}{dx}\right) = Q^- - Q^+, \tag{5}$$

where s represent the specific entropy of the flow. The specific internal energy (u) of the flow is expressed as

$$u = \frac{P_{\rm gas}}{\rho(\gamma-1)} + \frac{3P_{\rm rad}}{\rho}, \tag{6}$$

where γ denotes the adiabatic index, which we keep fixed as $4/3$ throughout this study. In Equation (5), Q^+ and Q^- represent the energy gain due to viscous heating and energy loss due to neutrino cooling, respectively. Following S. K. Chakrabarti & S. Das (2004), the heating term Q^+ is expressed as

$$Q^+ = Q_{\rm vis} = -\alpha(\Sigma v^2 + W)x\frac{d\Omega}{dx}, \tag{7}$$

whereas the cooling due to loss of neutrinos is obtained as (T. Di Matteo et al. 2002)

$$Q^- = Q_{\nu} = \sum_i \frac{(7/8)\sigma T^4}{(3/4)[\tau_{\nu_i}/2 + 1/\sqrt{3} + 1/(3\tau_{a,\nu_i})]}, \tag{8}$$

where τ_{ν_i} $[=\tau_{a,\nu_i}+\tau_{s,\nu_i}]$ is the sum of absorptive and scattering optical depths corresponding to each neutrino flavor. The index i refers to both electron-type neutrinos ν_e, $\bar{\nu}_e$ and heavy lepton neutrinos ν_μ, $\bar{\nu}_\mu$, ν_τ, and $\bar{\nu}_\tau$, while the subscript s and a are used to denote scattering and absorption, respectively. It is worth mentioning that Equation (8) is valid in both optically thin and thick limits for neutrinos. Neutrinos can be produced through neutronization and thermal emission via various types of reactions, which are briefly described below (T. Di Matteo et al. 2002).

(I) Electron–positron pair annihilation ($e^- + e^+ \rightarrow \nu_i + \bar{\nu}_i$) (T. Liu et al. 2007), where the neutrino cooling rate per unit volume is given by

$$q^-_{e^-e^+\rightarrow\nu_e+\bar{\nu}_e} \approx 3.4 \times 10^{33} T_{11}^9 \text{ erg cm}^{-3}\text{ s}^{-1}, \quad (9)$$

$$q^-_{e^-e^+\rightarrow\nu_\mu+\bar{\nu}_\mu} = q_{e^-e^+\rightarrow\nu_\tau+\bar{\nu}_\tau} \approx 0.7 \times 10^{33} T_{11}^9 \text{ erg cm}^{-3}\text{ s}^{-1}, \quad (10)$$

where the temperature of the flow is expressed as $T = T_{11} \times 10^{11}$ K, T_{11} being scaled temperature.

(II) The electron–positron pair capture on nuclei occurs through the reactions ($p + e^- \rightarrow n + \nu_e$ and $n + e^+ \rightarrow p + \bar{\nu}_e$), a process known as neutronization (T. Di Matteo et al. 2002). The corresponding cooling rate per unit volume is given by

$$q^-_{eN} = q^-_{e^-p} + q^-_{e^+n} = 9.0 \times 10^{33} \rho_{10} T_{11}^6 \text{ erg cm}^{-3}\text{ s}^{-1}, \quad (11)$$

where $\rho = \rho_{10} \times 10^{10}$ g cm^{-3}, ρ_{10} being scaled density.

(III) The nucleon–nucleon bremsstrahlung process, described by the reaction $n + n \rightarrow n + n + \nu_i + \bar{\nu}_i$, contributes as follows (S. Hannestad & G. Raffelt 1998):

$$q^-_{brem} \approx 1.5 \times 10^{27} \rho_{10}^2 T_{11}^{5.5} \text{ erg cm}^{-3}\text{ s}^{-1}. \quad (12)$$

(IV) The plasmon decay is associated with the decay rate of transverse plasmons, indicating that standard photons interact with the electron gas via the decay process $\tilde{\gamma} \longrightarrow \nu_e + \bar{\nu}_e$. The expression for $q^-_{plasmon}$ is given by M. Ruffert et al. (1996) as

$$q^-_{plasmon} \approx 1.5 \times 10^{32} \quad T_{11}^9 \gamma_p^6 \exp(-\gamma_p) \times (2 + 2\gamma_p + \gamma_p^2) \text{ erg cm}^{-3}\text{ s}^{-1} \quad (13)$$

where γ_p is defined as $\gamma_p = 5.565 \times 10^{-2}[(\pi^2 + \eta_e^2)/3]^{1/2}$ and $\eta_e = \mu_e/k_B T$, μ_e being the electron chemical potential.

Now, we introduce the various absorption optical depths for different neutrino species defined as

$$\tau_{a,\nu_e} = \frac{(q^-_{e^-e^+\rightarrow\nu_e+\bar{\nu}_e} + q^-_{eN} + q^-_{brem} + q^-_{plasmon})H}{4(7/8)\sigma T^4}, \quad (14)$$

$$\tau_{a,\nu_\mu} = \tau_{a,\nu_\tau} = \frac{(q^-_{e^-e^+\rightarrow\nu_\mu+\bar{\nu}_\mu} + q^-_{brem})H}{4(7/8)\sigma T^4}. \quad (15)$$

On the contrary, any type of scattering delays the free escape of neutrinos from the disk. Additionally, neutrinos are also scattered by nucleons as well, and the corresponding scattering optical depth is given by T. Di Matteo et al. (2002) as

$$\tau_{s,\nu_i} = 2.7 \times 10^{-7} T_{11}^2 \rho_{10} H. \quad (16)$$

Putting the above absorption and scattering optical depth expressions into Equation (8) and using Equations (1), (3), (4), and (5), we obtain the gradient of radial velocity as

$$\frac{dv}{dx} = \frac{\mathcal{N}(x, v, \lambda, \Theta)}{\mathcal{D}(x, v, \lambda, \Theta)}, \quad (17)$$

where $\Theta = k_B T/(m_e c^2)$. Furthermore, the gradient of angular momentum (λ) and temperature (Θ) is obtained as

$$\frac{d\lambda}{dx} = \lambda_{11}\frac{dv}{dx} + \lambda_{12}, \quad (18)$$

and

$$\frac{d\Theta}{dx} = \Theta_{11}\frac{dv}{dx} + \Theta_{12}, \quad (19)$$

where the explicit expressions of λ_{11}, λ_{12}, Θ_{11}, and Θ_{12} are given in Appendix A.

The accreting matter typically begins its journey from the outer edge of the disk with a very low (subsonic) radial velocity and ultimately crosses the black hole horizon with a velocity comparable to the speed of light. Along the streamline, the flow must pass through a critical point (x_c) where it smoothly transits from subsonic to supersonic speeds. At this critical point, the Equation (17) becomes indeterminate in the form $(dv/dx)_{x_c} = 0/0$, allowing us to derive the critical point condition as (S. K. Chakrabarti & S. Das 2004)

$$\mathcal{N}(x, v, \lambda, \Theta)_{x_c} = \mathcal{D}(x, v, \lambda, \Theta)_{x_c} = 0. \quad (20)$$

Since the flow remains smooth and continuous at each radius, (dv/dx) must be finite throughout, we apply L'Hôpital's rule to evaluate $(dv/dx)_{x_c}$. Generally, a physically acceptable critical point that astrophysical flow passes through yields two distinct values: one for accretion $(dv/dx)_{x_c} < 0$ and another for wind $(dv/dx)_{x_c} > 0$. The critical point formed closest to the black hole horizon (x_h) is referred to as the inner critical point (x_{in}), while the critical point located farther away is called the outer critical point (x_{out}).

3. Results

We self-consistently solve Equations (17)–(19) using the fourth-order Runge–Kutta method to derive the global accretion solutions around the black hole. For this, we specify the global flow parameters α, $\dot{m}$, and a_k. Further, we make use of critical point x_c and angular momentum (λ_c) at x_c as local parameters. Using these parameters, we solve Equation (20) to calculate v_c and Θ_c at x_c. Subsequently, we compute the local flow energy (ε_c) at x_c following $\varepsilon(x) = v^2/2 + h + \Phi^{eff}$, h being the enthalpy of the flow and is given by $h = u + P/\rho$. With these initial values of the flow variables (i.e., x_c, λ_c, v_c, Θ_c, α, $\dot{m}$), we integrate Equations (17)–(19) inward from x_c to the black hole horizon (x_h) and outward from x_c to the outer edge $x_{edge} = 1000$ for a chosen a_k values. Finally, we combine these two segments to obtain the global transonic accretion solution, which connects the black hole horizon to the outer edge of the disk.

3.1. Global Solutions of NDAF

In Figure 1(a), we present examples of accretion solutions where Mach number ($M = v/C_s$, C_s being sound speed) is plotted with radial distance (x). Here, we choose the local flow parameters at the inner critical point as $x_{in} = 1.2833$ and $\lambda_{in} = 2.1022$, and global parameters as $\alpha = 0.001$ and $a_k = 0.99$. For $\dot{m} = 10^{-5}$, we find $v_{in} = 0.3194$ and

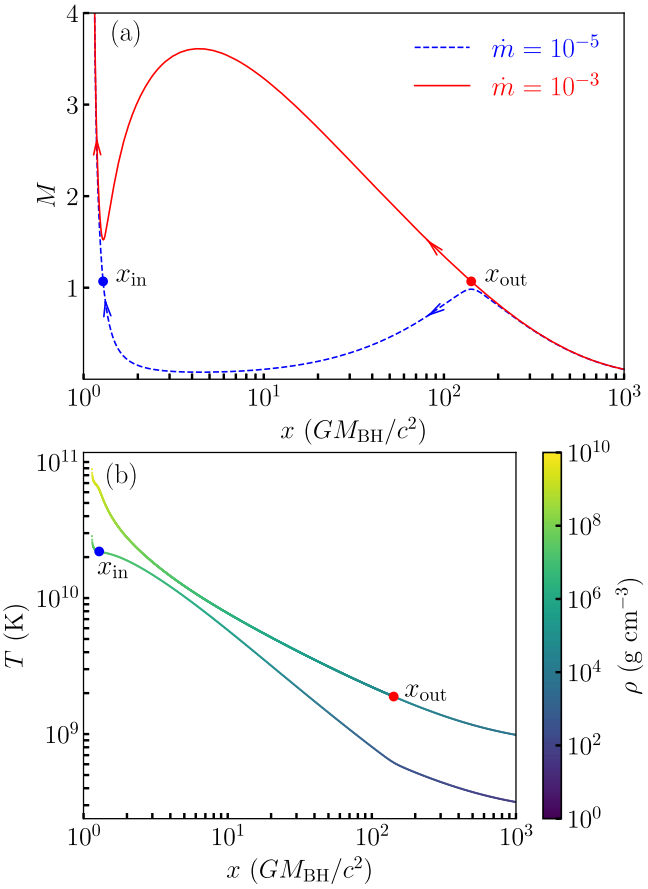

Figure 1. (a) Variation of Mach number ($M = v/C_s$) with radial distance (x) for different accretion rates ($\dot{m}$). NDAF injected from outer edge $x_{\rm edge} = 1000$ with $\varepsilon_{\rm edge} = 4.0668 \times 10^{-3}$, $\lambda_{\rm edge} = 2.4292$, $\alpha = 0.001$ around a black hole of spin $a_{\rm k} = 0.99$. Dashed (blue) and solid (red) curves represent the results for $\dot{m} = 10^{-5}$ and 10^{-3}, respectively. Critical points ($x_{\rm in}$ and $x_{\rm out}$) are marked, and arrows represent the direction of flow motion toward the black hole. (b) Temperature (T) variation of NDAF as a function of radial distance (x) for solutions presented in panel (a). Color indicates the density (ρ) variation with x where the color bar shows the range of density. See the main text for details.

$\Theta_{\rm in} = 3.7069$ at $x_{\rm in}$, yielding $\varepsilon_{\rm in} = 3.5054 \times 10^{-3}$, and the obtained result is plotted using a dashed (blue) curve. We note the flow variables at the outer edge of the disk at $x_{\rm edge} = 1000$ as $v_{\rm edge} = 3.8047 \times 10^{-3}$, $\lambda_{\rm edge} = 2.4292$, and $\Theta_{\rm edge} = 0.0533$, and compute the local energy $\varepsilon_{\rm edge} = 4.0668 \times 10^{-3}$. It is worth mentioning that one can get the identical accretion solution by integrating Equations (17)–(19) from $x_{\rm edge}$ toward the horizon using these outer boundary values of the accretion flow ($x_{\rm edge}$, $\varepsilon_{\rm edge}$, $\lambda_{\rm edge}$). Next, we increase the accretion rate as $\dot{m} = 10^{-3}$ while keeping the remaining flow variables ($\varepsilon_{\rm edge}$, $\lambda_{\rm edge}$, α, and $a_{\rm k}$) fixed at $x_{\rm edge} = 1000$ and compute the global transonic accretion solution by suitably tuning the velocity and temperature as $v_{\rm edge} = 3.8269 \times 10^{-3}$ and $\Theta_{\rm edge} = 0.0356$ that satisfy the critical point conditions (Equation (20)). We observe that the accretion solution alters its character as it passes through the outer critical point ($x_{\rm out} = 141.7357$) instead of the inner critical point ($x_{\rm in}$) with $\lambda_{\rm out} = 2.1092$, $v_{\rm out} = 0.0526$, and $\Theta_{\rm out} = 0.3180$. Thereafter, we again integrate Equations (17)–(19) inward from $x_{\rm out}$ to the horizon ($x_{\rm h}$) and obtain the global transonic accretion solution in the range of $x_{\rm h} < x \leqslant x_{\rm edge}$. This result is plotted using a solid (red) curve. In the figure, arrows indicate the direction of flow motion toward the black hole, and critical points ($x_{\rm in}$ and $x_{\rm out}$) are marked. In Figure 1(b), we show the temperature profiles of the NDAF solutions illustrated in Figure 1(a). For $\dot{m} = 10^{-5}$, the flow temperature reaches approximately $T \sim 3 \times 10^{10}$ K near the horizon, while for $\dot{m} = 10^{-3}$, the temperature exceeds $T \sim 9 \times 10^{10}$. The corresponding density profiles (ρ) are represented by color, with the color bar on the right indicating the range of flow density. It is evident from the figure that the flow density remains very high in the inner part of the disk for both cases, with values around $\rho \sim 10^{8-10}$ g cm^{-3}.

3.2. Shock-induced NDAF Solutions

In this section, we present for the first time the shock-induced global accretion solution in NDAFs. As indicated in Figure 1, the flow begins with negligible radial velocity, gradually increasing as it moves toward the black hole. During this journey, the flow undergoes a sonic state transition from subsonic to supersonic as it crosses the outer critical point ($x_{\rm out}$) before entering into the black hole. Interestingly, due to the rotation of matter, the flow experiences centrifugal repulsion during the accretion process. This leads to an accumulation of infalling matter, forming an effective boundary layer around the black hole. It is important to note that this accumulation of matter does not continue indefinitely as the centrifugal barrier triggers the discontinuous shock transition in the flow variables once the limiting threshold is reached (J. Fukue 1987; S. K. Chakrabarti 1989; S. Das & S. K. Chakrabarti 2004). Indeed, the global accretion solutions containing shock waves are thermodynamically preferred compared to shock-free solutions due to their higher entropy content (P. A. Becker & D. Kazanas 2001).

When accretion flow experiences shock transition, RHCs (L. D. Landau & E. M. Lifshitz 1959) must be satisfied. In the context of vertically integrated accretion flows, the RHCs are expressed as follows: (a) continuity of mass flux $\dot{M}_+ = \dot{M}_-$, (b) continuity of energy flux $\varepsilon_+ = \varepsilon_-$, and (c) continuity of momentum flux $\Pi_+ = \Pi_-$. Here, $\Pi (= W + \Sigma v^2)$ denotes the vertically integrated total pressure, and the quantities with subscripts "$-$" and "$+$" represent the flow variable just before and after the shock transition.

To examine the shock transition,[1] we make use of the accretion solutions passing through the outer critical point ($x_{\rm out}$) as shown in Figure 1. For this solution, we observe that after crossing the outer critical point, the supersonic flow undergoes discontinuous shock transition to the subsonic branch at $x_{\rm s} = 85.4376$, where RHCs are satisfied. After the shock, the slowly moving flow gradually gains its radial velocity as it proceeds inward and ultimately enters into the black hole after smoothly crossing the inner critical point at $x_{\rm in} = 1.2969$. The result of the shock-induced global accretion solution is depicted in the upper panel of Figure 2 using a solid (red) curve, where the vertical arrow indicates the shock transition radius. To examine the role of accretion rate ($\dot{m}$) on shock formation, we choose $\dot{m} = 5 \times 10^{-3}$, keeping other model parameters unchanged (i.e., $\varepsilon_{\rm edge} = 4.0668 \times 10^{-3}$, $\lambda_{\rm edge} = 2.4292$, $\alpha = 0.001$, and $a_{\rm k} = 0.99$). We find that shock forms at a lower radius $x_{\rm s} = 33.8093$, as illustrated by the dashed (blue) curve. This happens because a higher accretion rate increases both the density (ρ) (see Equation (3))) and the temperature (T) of the flow. Specifically, the increase in ρ and T leads to enhanced neutrino cooling (see Equation (8)), which pushes the shock

[1] See Appendix C for details.

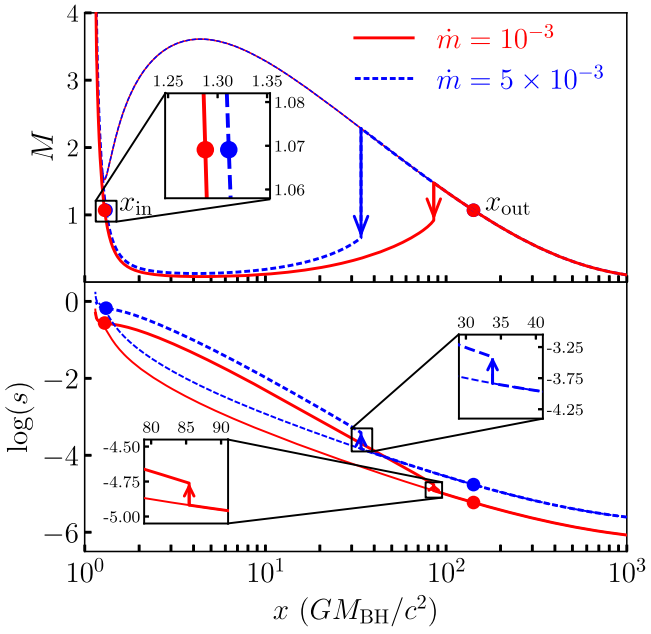

Figure 2. Examples of shock-induced global NDAF solutions obtained for different accretion rates ($\dot{m}$). Solid (red) and dashed (blue) curves denote results obtained for $\dot{m} = 10^{-3}$ and 5×10^{-3}, where vertical arrows indicate the shock radii $x_{\rm s} = 85.4376$ and $x_{\rm s} = 33.8093$. Here, the other model parameters are chosen to be the same as those used in Figure 1. See the main text for details.

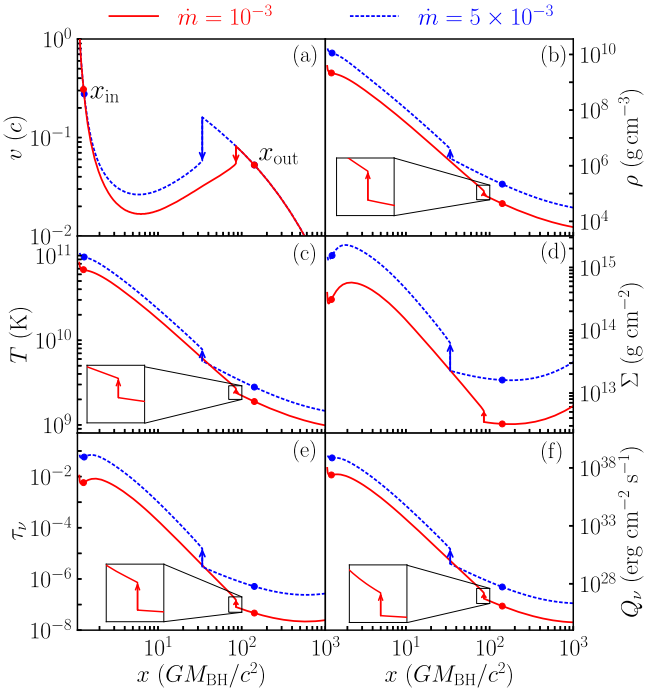

Figure 3. Radial variation of (a) radial velocity v, (b) mass density ρ, (c) temperature T, (d) surface density Σ, (e) neutrino optical depth, and (f) neutrino cooling Q_ν for shocked solutions presented in Figure 2. Solid (red) and dashed (blue) curves are for $\dot{m} = 10^{-3}$ and 5×10^{-3}, respectively. In each panel, filled circles indicate the critical points, and the shock transition is shown by a vertical arrow. See the main text for details.

front inward, where RHCs are satisfied. In the figure, arrows indicate the overall direction of the flow motion toward the black hole. In the lower panel of Figure 2, we present the variation of the specific entropy for both shocked and shock-free solutions, shown in the upper panel. Following S. Chandrasekhar (1939), S. Das et al. (2009), and S. Mitra & S. Das (2024), we compute the specific entropy of the flow as $s \propto P/\rho^{\gamma-1}$. We observe that the postshock flow possesses higher specific entropy as it increases across the shock front. With this, we emphasize that shocked accretion solutions are thermodynamically preferred over shock-free solutions.

In Figure 3, we depict the radial profiles of the flow variables corresponding to the shock-induced global accretion solutions presented in Figure 2. Solid (red) and dashed (blue) curves represent flow variables for $\dot{m} = 10^{-3}$ and 5×10^{-3}, respectively. In panel (a), we show the variation of radial velocity (v) with radial distance (x). We observe that v increases as matter accretes toward the black hole from the outer edge of the disk ($x_{\rm edge} = 1000$) and sharply decreases across the shock front, as shown by vertical arrows. However, due to the extreme gravitational attraction of the black hole, the flow subsequently gains its velocity and ultimately falls into the black hole horizon at supersonic speeds. Panel (b) illustrates the mass density profile ρ as a function of x. Due to shock, convergent flow experiences density compression at the postshock region (referred to as the postshock corona, or PSC), resulting in an increase in ρ. This increase of ρ occurs because the radial velocity of the flow decreases across the shock front, which causes the increase in density in order to conserve the mass flux, which is one of the fundamental conditions for shock transition. In panel (c), we display the variation of temperature (T) with x. A notable jump in temperature occurs across the shock, as the kinetic energy of the preshock flow is converted into thermal energy, leading to an increase in the postshock region. Panel (d) presents the radial variation of surface density (Σ), revealing that Σ rises at PSC due to the density compression occurring at the shock front. In panel (e), we present the neutrino optical depth. It is clear that the flow remains optically thin across the entire length scale, with $\tau_\nu < 1$, allowing neutrinos to escape easily from the disk. Finally, panel (f) illustrates the profile of neutrino cooling (in $\rm erg\,cm^{-2}\,s^{-1}$) as a function of radial distance, incorporating contributions from various processes discussed in Section 2. Given the higher temperature and density in the postshock region compared to the preshock region, it is evident that the net energy loss will be greater in the postshock flow.

3.3. Neutrino Luminosity ($\rm L_\nu$) and Neutrino Annihilation Luminosity ($L_{\nu\,\bar{\nu}}$)

Having established the global accretion solutions for NDAFs, we now turn our attention to estimating the neutrino radiation luminosity prior to the annihilation process. We calculate the neutrino radiation luminosity of the NDAF as (T. Liu et al. 2007)

$$L_\nu = 4\pi \int_{x_i}^{x_f} Q_\nu\, x\, dx, \tag{21}$$

where x_i denotes the radius just outside the horizon ($x_{\rm h}$), x_f refers to the outer edge of the disk ($x_{\rm edge}$) and Q_ν is the neutrino cooling rate expressed in units of $\rm erg\,cm^{-2}\,s^{-1}$. Following M. Ruffert et al. (1997), R. Popham et al. (1999), and S. Rosswog et al. (2003), we estimate the neutrino annihilation luminosity by dividing the disk into a grid of cells in the equatorial plane, with each cell characterized by its mean neutrino energy. The kth cell has a mean neutrino energy

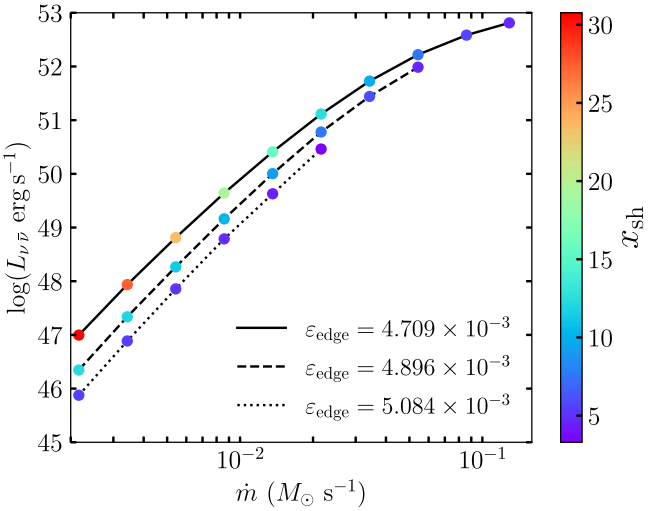

Figure 4. Variation of neutrino annihilation luminosity ($L_{\nu\bar{\nu}}$) with accretion rate ($\dot{m}$) for shocked solutions. Here, we fix the model parameters as ($a_{\rm k}$, α, $\lambda_{\rm edge}$) = (0.99, 0.001, 2.5331). Filled circles connected by solid, dashed, and dotted lines represent results corresponding to $\varepsilon_{\rm edge} = 4.709 \times 10^{-3}$, 4.834×10^{-3}, 4.959×10^{-3}, and 5.084×10^{-3}, respectively. Colors denote the shock radii. See the main text for details.

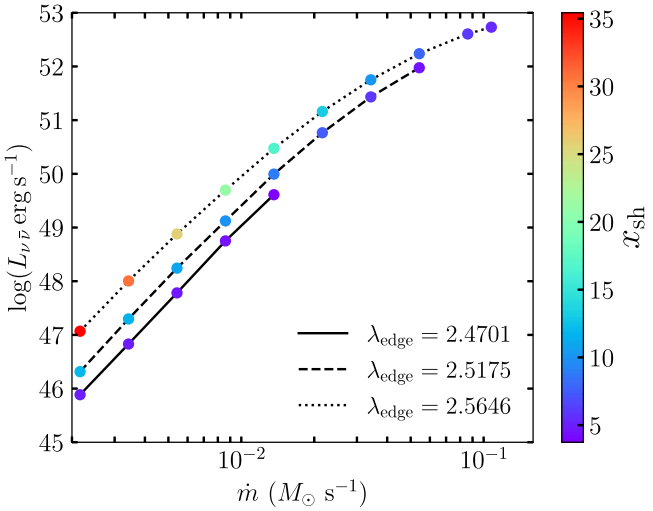

Figure 5. Variation of annihilation luminosity ($L_{\nu\bar{\nu}}$) with accretion rate ($\dot{m}$) for shocked solutions. Here, we fix the parameters as ($a_{\rm k}$, α, $\varepsilon_{\rm edge}$ = 0.99, 0.001, 4.834×10^{-3}). Filled circles connected by solid, dashed, and dotted lines represent results corresponding to $\lambda_{\rm edge}$ = 2.4701, 2.5175, and 2.5646, respectively. Colors denote the shock radii. See the main text for details.

denoted as $\epsilon^{\rm k}_{\nu_i}$ and a neutrino radiation luminosity of $l^{\rm k}_{\nu_i}$. The distance to a spatial point above (or below) the disk is represented by $d_{\rm k}$. The quantity $l^{\rm k}_{\nu_i}$ is calculated for each neutrino flavor in a cell through the surface integral of neutrino cooling (see Equation (21)). The angle at which neutrinos from cell k interact with antineutrinos from another cell k' is denoted by $\theta_{\rm k,k'}$. The energy deposition rate per unit volume (in units of erg cm^{-3} s^{-1}) at that point is given by

$$l_{\nu\bar{\nu}} = \sum_i A_{1,i} \sum_{\rm k} \frac{l^{\rm k}_{\nu_i}}{d^2_{\rm k}} \sum_{\rm k'} \frac{l^{\rm k'}_{\bar{\nu}_i}}{d^2_{\rm k'}} (\epsilon^{\rm k}_{\nu_i} + \epsilon^{\rm k'}_{\bar{\nu}_i})(1 - \cos\theta_{\rm k\,k'})^2 + \sum_i A_{2,i} \sum_{\rm k} \frac{l^{\rm k}_{\nu_i}}{d^2_{\rm k}} \sum_{\rm k'} \frac{l^{\rm k'}_{\bar{\nu}_i}}{d^2_{\rm k'}} \frac{\epsilon^{\rm k}_{\nu_i} + \epsilon^{\rm k'}_{\bar{\nu}_i}}{\epsilon^{\rm k}_{\nu_i} \epsilon^{\rm k'}_{\bar{\nu}_i}} (1 - \cos\theta_{\rm k\,k'}). \quad (22)$$

In Equation (22), the explicit expression of $A_{1,i}$ and $A_{2,i}$ are given in Appendix B. We calculate the total neutrino annihilation luminosity by integrating over the entire region outside the black hole and the disk, as described in L. Xue et al. (2013), and is expressed as

$$L_{\nu\bar{\nu}} = 4\pi \int_{x_i}^{\infty} \int_{H}^{\infty} l_{\nu\bar{\nu}} x\,dx\,dz, \quad (23)$$

where z refers to the vertical axis.

In Figure 4, we present the variation of $L_{\nu\bar{\nu}}$ as a function of accretion rate ($\dot{m}$) for different $\varepsilon_{\rm edge}$. Here, we choose $\lambda_{\rm edge}$ = 2.5331, α = 0.001, and $a_{\rm k}$ = 0.99. Filled circles connected with solid, dashed, and dotted lines are obtained for $\varepsilon_{\rm edge} = 4.709 \times 10^{-3}$, 4.896×10^{-3}, and 5.084×10^{-3}, respectively. Colors represent the shock radii, with the range indicated by the color bar on the right side of the figure. Notably, when $\varepsilon_{\rm edge}$ is relatively smaller, shock forms over a broader, whereas larger values of $\varepsilon_{\rm edge}$ result in a more limited range for shock formation. We observe that for a given $\varepsilon_{\rm edge}$, $L_{\nu\bar{\nu}}$ increases with $\dot{m}$. This behavior can be attributed to the fact that the density of the flow increases with the accretion rate. As density rises, neutrino cooling in the flow is enhanced, which in turn leads to an increase in luminosity. On the contrary, for a fixed $\dot{m}$, $L_{\nu\bar{\nu}}$ decreases with the increase of $\varepsilon_{\rm edge}$. This occurs because an increase in $\varepsilon_{\rm edge}$ causes the shock front to shift toward the horizon, resulting in a reduction in the size of the postshock region (PSC). Consequently, this leads to a decrease in $L_{\nu\bar{\nu}}$.

Next, we compare the neutrino annihilation luminosity $L_{\nu\bar{\nu}}$ for flows injected with different $\lambda_{\rm edge}$ values. The obtained results are presented in Figure 5, where $L_{\nu\bar{\nu}}$ is plotted with $\dot{m}$. Here, we choose $\varepsilon_{\rm edge} = 4.834 \times 10^{-3}$, $\alpha = 0.001$, and $a_{\rm k} = 0.99$. In the figure, filled circles joined with solid, dashed, and dotted lines denote results corresponding to $\lambda_{\rm edge}$ = 2.4701, 2.5175, and 2.5646, respectively. The colors indicate the shock radii with the range illustrated by the color bar. It is evident that $L_{\nu\bar{\nu}}$ increases with $\dot{m}$ for a fixed $\lambda_{\rm edge}$. Furthermore, when $\dot{m}$ is held constant, $L_{\nu\bar{\nu}}$ also increases for higher values of $\lambda_{\rm edge}$, as this enlarges the size of the PSC due to the larger shock radius.

Thereafter, we put forth efforts to estimate the maximum neutrino luminosity $L_{\nu}^{\rm max}$ and maximum neutrino annihilation luminosity $L_{\nu\bar{\nu}}^{\rm max}$ using our model formalism. In order to do that, we choose α = 0.005 and compute $L_{\nu}^{\rm max}$ and $L_{\nu\bar{\nu}}^{\rm max}$ for weakly rotating ($a_{\rm k} \to 0$) as well as rapidly rotating ($a_{\rm k} \to 1$) black holes by freely varying both $\varepsilon_{\rm edge}$ and $\lambda_{\rm edge}$. The obtained results are depicted in Figure 6, open circles and open squares joined with solid and dashed lines denote the variation of $L_{\nu}^{\rm max}$ and $L_{\nu\bar{\nu}}^{\rm max}$ with accretion rate $\dot{m}$ for $a_{\rm k}$ = 0 and $a_{\rm k}$ = 0.99, respectively. Overall, we observe that as the accretion rate increases, both luminosities rise. This is attributed to the enhancement of flow density, which allows matter to cool more efficiently. Additionally, we find that for a fixed $\dot{m}$, the luminosity is consistently higher for greater spin. From this analysis, we infer that the shock-induced global NDAF formalism is potentially promising for explaining the exceedingly high neutrino luminosity, as it is derived from a wide range of model parameters (α, $\dot{m}$, $a_{\rm k}$).

4. Astrophysical Implications

In this section, we apply our model formalism to elucidate the energy output associated with the annihilation luminosity of GRBs. To achieve this, we select five GRBs for which the isotropic radiated energy during the prompt emission phase ($E_{\gamma,\rm iso}$), the isotropic kinetic energy of the outflow powering the

Table 1
Observable Parameters of the GRBs Being Studied

Source	T_{90} (s)	z'	$E_{\gamma,\rm iso}$ ($\times 10^{51}$ erg)	$E_{\rm k,iso}$ ($\times 10^{51}$ erg)	$\theta_{\rm j}$ (rad)	$\dot{E}$ (erg s^{-1})	$L_{\nu,\bar{\nu}}^{\rm obs}$ (erg s^{-1})	References
GRB 071227	1.80	0.381	0.080	0.25	∼0.05	3.1×10^{47}	3.1×10^{48}	T. Liu et al. (2015)
GRB 051210	1.30	1.300	0.360	2.38	∼0.05	6.1×10^{48}	6.1×10^{49}	T. Liu et al. (2015)
GRB 130603B	0.18	0.356	0.200	2.80	∼0.07	4.3×10^{49}	4.3×10^{50}	W. Fong & E. Berger (2013)
GRB 140622A	0.13	0.959	0.065	9.77	∼0.05	3.3×10^{50}	3.3×10^{51}	T. Liu et al. (2015)
GRB 090426	1.20	2.609	2.840	135.00	∼0.07	1.9×10^{51}	1.9×10^{52}	A. Nicuesa Guelbenzu et al. (2011)

Note. In columns (1)−(9), GRB sources, burst duration (T_{90}), redshift (z'), $E_{\gamma,\rm iso}$, $E_{\rm k,iso}$, opening angle ($\theta_{\rm j}$), GRB output power ($\dot{E}$), annihilation luminosity ($L_{\nu,\bar{\nu}}^{\rm obs}$), and references are presented.

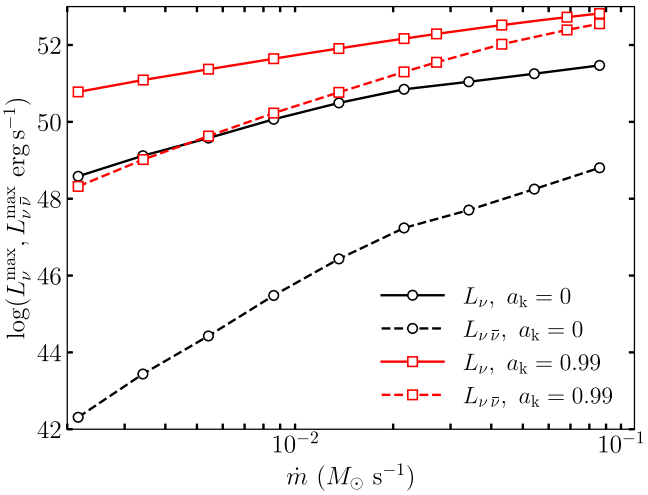

Figure 6. Variation of maximum neutrino luminosity ($L_\nu^{\rm max}$) and neutrino annihilation luminosity ($L_{\nu\bar{\nu}}^{\rm max}$) with accretion rate $\dot{m}$ for different $a_{\rm k}$ values. Here, we choose the viscosity parameter as $\alpha = 0.005$. Open circles (black) connected by solid and dashed lines represent $L_\nu^{\rm max}$ and $L_{\nu\bar{\nu}}^{\rm max}$ for a nonrotating ($a_{\rm k} = 0$) black hole, whereas open squares (red) connected by solid and dashed lines indicate $L_\nu^{\rm max}$ and $L_{\nu\bar{\nu}}^{\rm max}$ for a rotating ($a_{\rm k} = 0.99$) black hole. See the main text for details.

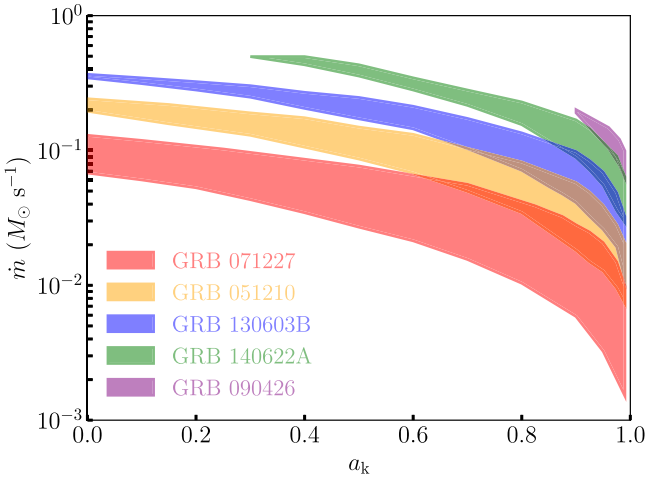

Figure 7. Effective domain of parameters in $a_{\rm k}$–$\dot{m}$ plane that satisfactorily explains $L_{\nu\bar{\nu}}^{\rm obs}$ for GRB sources 071227 (red), 051210 (orange), 130603B (blue), 140622A (green), and 090426 (purple) is illustrated. See the main text for details.

afterglow phase ($E_{\rm k,iso}$), the opening angle of the ejecta $\theta_{\rm j}$, the duration of the burst (T_{90}), and the redshift (z') are known from the literature (A. Nicuesa Guelbenzu et al. 2011; W. Fong & E. Berger 2013; T. Liu et al. 2015). Using these observational data, we estimate the mean fireball output power from the central engine ($\dot{E}$) of the GRB as described in Y.-Z. Fan & D.-M. Wei (2011) and T. Liu et al. (2015), which is given by

$$\dot{E} \approx \frac{(1+z')(E_{\gamma,\rm iso} + E_{\rm k,iso})\theta_{\rm j}^2}{2T_{90}}. \tag{24}$$

For the selected GRBs being studied, we observe a wide range of energy release rates as $\dot{E} \sim 10^{47-52}$ erg s^{-1} (see Table 1).

Meanwhile, the simulation results for GRBs suggest that $\dot{E}$ is a fraction of the neutrino annihilation luminosity. Consequently, the observed neutrino annihilation luminosity ($L_{\nu\bar{\nu}}^{\rm obs}$) of GRBs can be estimated as follows (M. A. Aloy et al. 2005):

$$L_{\nu\bar{\nu}}^{\rm obs} = \dot{E}/\eta, \tag{25}$$

where η denotes the efficiency of energy conversion by neutrino-antineutrino annihilation. It is worth noting that the plausible estimate of the η value is not well-constrained due to persistent uncertainties in the efficiency (T. Liu et al. 2015). Therefore, we adopt a reasonable estimate of $\eta = 0.1$ for illustrative purposes. We present the observational properties of the GRB sources being studied in Table 1.

To explain the observed neutrino annihilation luminosity $L_{\nu\bar{\nu}}^{\rm obs}$ of GRBs, we theoretically compute $L_{\nu\bar{\nu}}$ (see Equation (23)). Indeed, the precise estimates of mass ($M_{\rm BH}$), spin ($a_{\rm k}$), and accretion rate ($\dot{m}$) for GRB sources remain uncertain, as these quantities have not been conclusively determined. Hence, in this work, we adopt a reasonable estimate of source mass as $M_{\rm BH} = 3M_\odot$, and compute $L_{\nu\bar{\nu}}$ across a range of $a_{\rm k}$ and $\dot{m}$. This is achieved by varying model parameters, including energy, angular momentum, and viscosity of the flow. The results obtained are illustrated in Figure 7, where the bounded regions in the $a_{\rm k}$–$\dot{m}$ plane correspond to the observed $L_{\nu\bar{\nu}}^{\rm obs}$ values for each GRB source. The regions shaded in red, orange, blue, green, and purple are for GRB 071227 ($L_{\nu\bar{\nu}}^{\rm obs} = 3.1 \times 10^{48}$ erg s^{-1}), GRB 051210 ($L_{\nu\bar{\nu}}^{\rm obs} = 6.1 \times 10^{49}$ erg s^{-1}), GRB 130603B ($L_{\nu\bar{\nu}}^{\rm obs} = 4.3 \times 10^{50}$ erg s^{-1}), GRB 140622A ($L_{\nu\bar{\nu}}^{\rm obs} = 3.3 \times 10^{51}$ erg s^{-1}), and GRB 090426 ($L_{\nu\bar{\nu}}^{\rm obs} = 1.9 \times 10^{52}$ erg s^{-1}), respectively. For GRB 071227, GRB 051210, and GRB 130603B, the computed range of accretion rates are $0.0015 \lesssim \dot{m} \lesssim 0.13$, $0.0073 \lesssim \dot{m} \lesssim 0.24$ and $0.011 \lesssim \dot{m} \lesssim 0.37$, respectively, encompassing the spin range of $0 \leqslant a_{\rm k} < 1$. In contrast, for GRB 140622A, the central source appears to be rotating either moderately or rapidly, with

$0.3 \leqslant a_{\rm k} < 0.99$ and an accretion rate in the range of $0.03 \lesssim \dot{m} \lesssim 0.5$. Furthermore, for GRB 090426, the source is found to be rapidly rotating, with $a_{\rm k} > 0.9$ and $0.06 \lesssim \dot{m} \lesssim 0.2$. These findings evidently suggest that rapidly rotating black holes seem to be more favorable in explaining the energy outputs of GRBs.

5. Conclusions

In this investigation, we explore steady, axisymmetric NDAFs surrounding rotating black holes. By incorporating neutrino cooling (Q_ν), we solve the governing equations in a self-consistent manner and identify transonic solutions, both with and without shocks, for a specified set of flow parameters ($\dot{m}$, α, $a_{\rm k}$, $\varepsilon_{\rm edge}$, $\lambda_{\rm edge}$) that comply with the inner boundary condition. Additionally, we derive accretion solutions that manifest shock phenomena under the same parameter conditions. These shocked solutions seem to be more viable than the shock-free solutions, as previously discussed in P. A. Becker & D. Kazanas (2001). Our key findings are summarized below.

1. We find that global transonic NDAFs exist that pass through either inner ($x_{\rm in}$) or outer ($x_{\rm out}$) critical points for the first time, to the best of our knowledge. Our analysis demonstrates that by varying the accretion rate $\dot{m}$ while keeping other flow parameters constant at the outer edge ($x_{\rm edge}$), the character of the solutions changes as they pass $x_{\rm out}$ rather than $x_{\rm in}$. Notably, we observe that close to the horizon, the temperature (T) and density (ρ) of the NDAF exceed $T \gtrsim 10^{10}\,{\rm K}$ and $\rho \gtrsim 10^{8}\,{\rm g\,cm^{-3}}$, which are favorable for neutrino emission (R. Popham et al. 1999) (see Figure 1).
2. We obtain the shock-induced global transonic solutions in the realm of NDAFs at remarkably high accretion rates (see Figure 2). Our findings indicate that the PSC is characterized by increased density and elevated temperatures compared to the preshock flow, creating a highly radiative environment conducive to substantial neutrino emission (see Figure 3).
3. We also investigate the impact of $\dot{m}$, $\varepsilon_{\rm edge}$, $\lambda_{\rm edge}$ on the annihilation luminosity ($L_{\nu\bar{\nu}}$) for shocked solutions. Our analysis demonstrates that $L_{\nu\bar{\nu}}$ exhibits an increasing trend with $\dot{m}$ when flow parameters (α, $\varepsilon_{\rm edge}$, $\lambda_{\rm edge}$, $a_{\rm k}$) are held fixed (see Figures 4 and 5). This enhancement is attributed to the increased density of the flow as $\dot{m}$ increases, yielding a more radiative environment in NDAFs.
4. Furthermore, we compute the maximum neutrino luminosity $L_{\nu}^{\rm max}$ and maximum neutrino annihilation luminosity $L_{\nu\bar{\nu}}^{\rm max}$, examining how these quantities vary with accretion rate ($\dot{m}$) for weakly ($a_{\rm k} \to 0$) and rapidly ($a_{\rm k} \to 1$) rotating black holes (see Figure 6). Our findings reveal that both $L_{\nu}^{\rm max}$ and $L_{\nu\bar{\nu}}^{\rm max}$ exhibit a positive correlation with $\dot{m}$ for fixed values of $a_{\rm k}$, and that higher $a_{\rm k}$ results in enhanced luminosities for a given accretion rate.
5. We employ our model formalism to explain the neutrino annihilation luminosity $L_{\nu\bar{\nu}}^{\rm obs}$ (see Equation (25)) observed from the GRBs. We find that a shock-induced global NDAF model satisfactorily accounts for $L_{\nu\bar{\nu}}$, corresponding to the energy release rates of five GRBs, which range from $\dot{E} \sim 10^{47-52}\,{\rm erg\,s^{-1}}$. Based on these findings, we infer the potential range of accretion rates for the GRBs, considering parameters such as $a_{\rm k}$ and $M_{\rm BH}$. We find that for $0 \leqslant a_{\rm k} < 1$ and $M_{\rm BH} = 3M_\odot$, the accretion rates for GRB 071227, GRB 051210, and GRB 130603B are $0.0015 \lesssim \dot{m} \lesssim 0.13$, $0.0073 \lesssim \dot{m} \lesssim 0.24$, and $0.011 \lesssim \dot{m} \lesssim 0.37$, respectively. For GRB 140622A, we obtain $0.03 \lesssim \dot{m} \lesssim 0.5$ for $0.3 \leqslant a_{\rm k} < 0.99$ and $M_{\rm BH} = 3M_\odot$. On the contrary, the central source of GRB 090426 ($M_{\rm BH} = 3M_\odot$) appears to be rapidly rotating ($a_{\rm k} > 0.9$) and accreting within the range of $0.06 \lesssim \dot{m} \lesssim 0.2$ (see Figure 7).

Finally, we mention that for the first time, to the best of our knowledge, we explore the shock-induced global NDAFs around rotating stellar-mass black holes to explain the neutrino annihilation luminosity of GRBs. It is important to note that the present formalism relies on several approximations. We adopt an effective potential to mimic the spacetime geometry around a rotating black hole, rather than working within a general relativistic framework. We do not consider magnetic fields, even though they are ubiquitous in all astrophysical environments. We ignore the effects of self-gravity as well. Implementation of these physical processes is beyond the scope of this study and we intend to investigate them in future research.

Acknowledgments

The work of A.K. is supported by the Council and Scientific & Industrial Research, India. S.C. thanks MATRICS, Science and Engineering Research Board (SERB), India, for support through grant MTR/2022/000318. S.D. acknowledges financial support from MATRICS, SERB, India, through grant MTR/2020/000331.

Data Availability

The data underlying this article will be available upon reasonable request.

Appendix A
Expressions for $\mathcal{N}$, $\mathcal{D}$, λ_{11}, λ_{12}, Θ_{11}, Θ_{12}

The equations of radial momentum (1), mass conservation (3), azimuthal momentum (4), and entropy generation Equation (5) can be combinedly expressed as

$$\mathcal{A}_\lambda \frac{d\lambda}{dx} + \mathcal{A}_\Theta \frac{d\Theta}{dx} + \mathcal{A}_v \frac{dv}{dx} + \mathcal{A}_x = 0, \tag{A1}$$

$$\mathcal{B}_\lambda \frac{d\lambda}{dx} + \mathcal{B}_\Theta \frac{d\Theta}{dx} + \mathcal{B}_v \frac{dv}{dx} + \mathcal{B}_x = 0, \tag{A2}$$

$$\mathcal{C}_\lambda \frac{d\lambda}{dx} + \mathcal{C}_\Theta \frac{d\Theta}{dx} + \mathcal{C}_v \frac{dv}{dx} + \mathcal{C}_x = 0, \tag{A3}$$

where the coefficients $\mathcal{A}_j$, $\mathcal{B}_j$, and $\mathcal{C}_j$, $j \to \lambda$, Θ, v, x, in the above equations are functions of x, v, λ, and Θ. Using Equations (A1)–(A3), we obtain Equations (17)–(19) and the

coefficients involved in these equations are given by

$$\mathcal{N} = \mathcal{C}_x\mathcal{A}_\Theta\mathcal{B}_\lambda - \mathcal{C}_\Theta\mathcal{A}_x\mathcal{B}_\lambda - \mathcal{C}_x\mathcal{A}_\lambda\mathcal{B}_\Theta + \mathcal{C}_\lambda\mathcal{A}_x\mathcal{B}_\Theta + \mathcal{C}_\Theta\mathcal{A}_\lambda\mathcal{B}_x - \mathcal{C}_\lambda\mathcal{A}_\Theta\mathcal{B}_x,$$
$$\mathcal{D} = -\mathcal{C}_v\mathcal{A}_\Theta\mathcal{B}_\lambda + \mathcal{C}_\Theta\mathcal{A}_v\mathcal{B}_\lambda + \mathcal{C}_v\mathcal{A}_\lambda\mathcal{B}_\Theta - \mathcal{C}_\lambda\mathcal{A}_v\mathcal{B}_\Theta - \mathcal{C}_\Theta\mathcal{A}_\lambda\mathcal{B}_v + \mathcal{C}_\lambda\mathcal{A}_\Theta\mathcal{B}_v,$$
$$\lambda_{11} = \frac{\mathcal{A}_x\mathcal{B}_\Theta - \mathcal{A}_\Theta\mathcal{B}_x}{\mathcal{A}_\Theta\mathcal{B}_\lambda - \mathcal{A}_\lambda\mathcal{B}_\Theta}, \quad \lambda_{12} = \frac{\mathcal{A}_v\mathcal{B}_\Theta - \mathcal{A}_\Theta\mathcal{B}_v}{\mathcal{A}_\Theta\mathcal{B}_\lambda - \mathcal{A}_\lambda\mathcal{B}_\Theta},$$
$$\Theta_{11} = \frac{-\mathcal{A}_x\mathcal{B}_\lambda + \mathcal{A}_\lambda\mathcal{B}_x}{\mathcal{A}_\Theta\mathcal{B}_\lambda - \mathcal{A}_\lambda\mathcal{B}_\Theta}, \quad \Theta_{12} = \frac{-\mathcal{A}_v\mathcal{B}_\lambda + \mathcal{A}_\lambda\mathcal{B}_v}{\mathcal{A}_\Theta\mathcal{B}_\lambda - \mathcal{A}_\lambda\mathcal{B}_\Theta},$$

where

$$\mathcal{A}_\lambda = 1 + \lambda_1\Theta_1, \quad \mathcal{A}_\Theta = \lambda_1\Theta_2,$$
$$\mathcal{A}_v = \frac{A_1S_1}{v\ C_{s0}}, \quad \mathcal{A}_x = \lambda_2 + \lambda_1\Theta_3,$$
$$\mathcal{B}_\lambda = R_1 + R_2\Theta_1, \quad \mathcal{B}_\Theta = R_2\Theta_2,$$
$$\mathcal{B}_v = R_3 + R_2\Theta_4, \quad \mathcal{B}_x = R_4 + R_2\Theta_3,$$
$$\mathcal{C}_\lambda = \mathcal{T}_1 - C_s^2v\mathcal{T}_2, \quad \mathcal{C}_\Theta = \mathcal{T}_3 - C_s^2v\mathcal{T}_4,$$
$$\mathcal{C}_v = \mathcal{T}_5 - C_s^2v\mathcal{T}_6, \quad \mathcal{C}_x = \mathcal{T}_7 - C_s^2v\mathcal{T}_8,$$
$$\lambda_1 = -\frac{2C_sx\alpha}{v}, \quad \Theta_1 = \frac{-C_sA_1S_1\mathcal{F}_1}{2\mathcal{F}(2C_s^2 - A_1S_1)}, \quad A_1 = \frac{11\pi\bar{a}c^3M_{BH}^2m_e^2}{3k_B\dot{M}},$$
$$S_1 = vH\Theta^4\sqrt{\Delta}, \quad \mathcal{F}_1 = g_1\frac{(\lambda \quad \Omega_\lambda + \Omega)}{(1-\lambda\Omega)^2},$$
$$g_1 = \frac{(x^2+a_k^2)^2 + 2\Delta a_k^2}{(x^2+a_k^2)^2 - 2\Delta a_k^2}, \quad \Omega_\lambda = \frac{\partial\Omega}{\partial\lambda}, \quad C_s = \frac{Y_1 + \sqrt{Y_1^2 + 4Y_2}}{2},$$
$$Y_1 = A_1v\sqrt{\frac{\Delta x^3}{\mathcal{F}}}\Theta^4, \quad Y_2 = \frac{m_e}{m_p}\Theta,$$
$$\lambda_2 = \frac{\alpha(C_s^2+v^2)}{v}\left(\frac{x}{2}\frac{\Delta'}{\Delta} - 2\right),$$
$$\Delta' = \frac{d\Delta}{dx}, \quad \Theta_3 = \frac{A_1S_1}{C_{s0}}\left(\frac{3}{2x} - \frac{\mathcal{F}_2}{2\mathcal{F}}\right) + \frac{S_1A_1\Delta'}{2C_{s0}\sqrt{\Delta}}, \quad C_{s0} = 2C_s - \frac{A_1S_1}{C_s},$$
$$\mathcal{F}_2 = \frac{1}{1-\lambda\Omega}\left(\frac{dg_1}{dx} + \gamma_\phi^2\lambda g_1\frac{d\Omega}{dx}\right), \quad R_1 = C_s^2\frac{\mathcal{F}_1}{2\mathcal{F}},$$
$$R_2 = C_s, \quad R_3 = v - \frac{C_s^2}{v}, \quad \Theta_4 = \frac{A_1S_1}{vC_{s0}},$$
$$R_4 = \frac{d\Phi^{\rm eff}}{dx} + C_s^2\left(\frac{\mathcal{F}_2}{2\mathcal{F}} - \frac{\Delta'}{2\Delta} - \frac{3}{2x}\right),$$
$$\mathcal{T}_1 = \Gamma_1 - 3A_1S_1v\left(\frac{\mathcal{F}_1}{2\mathcal{F}} + \frac{\Theta_1}{C_s}\right),$$
$$\Gamma_1 = -\alpha(v^2 + C_s^2)x\Omega_\lambda,$$
$$\mathcal{T}_2 = \frac{\mathcal{F}_1}{2\mathcal{F}} - \frac{\Theta_1}{C_s}, \quad \mathcal{T}_3 = \frac{v}{\gamma-1}\frac{m_e}{m_p} + 3A_1S_1v\left(\frac{4}{\Theta} + \frac{\Theta_2}{C_s}\right),$$
$$\mathcal{T}_4 = -\frac{\Theta_2}{C_s}, \quad \mathcal{T}_5 = 3A_1S_1 + \frac{3A_1S_1\Theta_4v}{C_s}, \quad \mathcal{T}_6 = -\frac{\Theta_4}{C_s} - \frac{1}{v},$$
$$\mathcal{T}_7 = \Gamma_2 - \frac{\mathcal{Q}_\nu}{\Sigma} + \mathcal{C}_1, \quad \Gamma_2 = -\alpha(v^2 + C_s^2)x\frac{d\Omega}{dx},$$
$$\mathcal{C}_1 = \frac{3A_2S_1v}{2}\left(\frac{\Delta'}{\Delta} - \mathcal{F}\mathcal{F}_2 + \frac{2\Theta_3}{C_s} + \frac{3}{x}\right),$$
$$\mathcal{T}_8 = -\frac{\Theta_3}{C_s} + \frac{\mathcal{F}_2}{2\mathcal{F}} - \frac{\Delta'}{2\Delta} - \frac{3}{2x}.$$

Appendix B
Constants in Energy Deposition Rate $l_{\nu\bar{\nu}}$

In Equation (22), the constants $A_{1,i}$ and $A_{2,i}$ are given by (M. Ruffert et al. 1997; S. Rosswog et al. 2003)

$$A_{1,i} = \frac{\sigma_0}{12\pi^2\ c(m_ec^2)^2}[(C_{V,\nu_i} - C_{A,\nu_i})^2 + (C_{V,\nu_i} + C_{A,\nu_i})^2]$$

and $$A_{2,i} = \frac{\sigma_0}{6\pi^2c}(2C_{V,\nu_i}^2 - C_{A,\nu_i}^2),$$

where $\sigma_0 = 1.76 \times 10^{-44}\,\mathrm{cm}^2$, $C_{V,\nu_e} = \frac{1}{2} + 2\sin^2\theta_W$, $C_{V,\nu_\mu} = C_{V,\nu_\tau} = -\frac{1}{2} + 2\sin^2\theta_W$, $C_{A,\nu_e} = C_{A,\bar{\nu}_\mu} = C_{A,\bar{\nu}_\tau} = \frac{1}{2}$, $C_{A,\bar{\nu}_e} = C_{A,\nu_\mu} = C_{A,\nu_\tau} = -\frac{1}{2}$, and $\sin^2\theta_W = 0.23$.

Appendix C
Method of Calculating Accretion Solution with Shock

Here, we describe the methodology employed to obtain the shock solution.

1. For an accretion solution originating at $x_{\rm edge}$ and passing through the outer critical point ($x_{\rm out}$), we evaluate the total pressure Π, accretion rate $\dot{M}$, and local energy ε using the supersonic flow variables at a radial coordinate x, where $x < x_{\rm out}$.
2. We make use of RHCs (i.e., the conservation of Π, $\dot{M}$, and ε) to obtain three algebraic equations and solve them to calculate subsonic flow variables.
3. Using these subsonic flow variables, we numerically integrate Equations (17)–(19) toward the black hole and check the critical point conditions (Equation (20)).
4. If critical point conditions are satisfied, we obtain the inner critical point ($x_{\rm in}$, see Figure 2) and use the inner critical point flow variables to integrate Equations (17)–(19) all the way to the horizon $x_{\rm h}$. This yields a complete global accretion solution with a shock connecting $x_{\rm h}$ and $x_{\rm edge}$.
5. When critical point conditions are not satisfied, we decrease the radial coordinate x and repeat the process (points 1–4) until a complete accretion solution with a shock is found.

ORCID iDs

Santabrata Das https://orcid.org/0000-0003-4399-5047

References

Aktar, R., Das, S., Nandi, A., & Sreehari, H. 2017, MNRAS, 471, 4806
Aloy, M. A., Janka, H. T., & Müller, E. 2005, A&A, 436, 273
Becker, P. A., & Kazanas, D. 2001, ApJ, 546, 429
Chakrabarti, S. K. 1989, ApJ, 347, 365
Chakrabarti, S. K., & Das, S. 2004, MNRAS, 349, 649
Chakrabarti, S. K., & Molteni, D. 1993, ApJ, 417, 671
Chakrabarti, S. K., & Molteni, D. 1995, MNRAS, 272, 80
Chandrasekhar, S. 1939, An Introduction to the Study of Stellar Structure (New York: Dover)
Chen, B.-G., Liu, T., Qi, Y.-Q., et al. 2022, ApJ, 941, 156
Das, S. 2007, MNRAS, 376, 1659
Das, S., Becker, P. A., & Le, T. 2009, ApJ, 702, 649
Das, S., & Chakrabarti, S. 2004, IJMPD, 13, 1955
Das, S., Chattopadhyay, I., & Chakrabarti, S. K. 2001, ApJ, 557, 983
Das, S., Chattopadhyay, I., Nandi, A., & Molteni, D. 2014, MNRAS, 442, 251
Dihingia, I. K., Das, S., Maity, D., & Chakrabarti, S. 2018a, PhRvD, 98, 083004
Dihingia, I. K., Das, S., & Mandal, S. 2018b, MNRAS, 475, 2164
Dihingia, I. K., Das, S., & Nandi, A. 2019, MNRAS, 484, 3209
Di Matteo, T., Perna, R., & Narayan, R. 2002, ApJ, 579, 706
Eichler, D., Livio, M., Piran, T., & Schramm, D. N. 1989, Natur, 340, 126
Fan, Y.-Z., & Wei, D.-M. 2011, ApJ, 739, 47
Fong, W., & Berger, E. 2013, ApJ, 776, 18
Frank, J., King, A., & Raine, D. J. 2002, Accretion Power in Astrophysics (3rd ed.; Cambridge: Cambridge Univ. Press),
Fukue, J. 1987, PASJ, 39, 309
Hannestad, S., & Raffelt, G. 1998, ApJ, 507, 339
Janiuk, A., Yuan, Y., Perna, R., & Di Matteo, T. 2007, ApJ, 664, 1011
Kawanaka, N., & Mineshige, S. 2007, ApJ, 662, 1156

Kohri, K., & Mineshige, S. 2002, ApJ, 577, 311
Kohri, K., Narayan, R., & Piran, T. 2005, ApJ, 629, 341
Kouveliotou, C., Meegan, C. A., Fishman, G. J., et al. 1993, ApJL, 413, L101
Landau, L. D., & Lifshitz, E. M. 1959, Fluid Mechanics (Oxford: Pergamon),
Liu, T., Gu, W.-M., Xue, L., & Lu, J.-F. 2007, ApJ, 661, 1025
Liu, T., Gu, W.-M., & Zhang, B. 2017, NewAR, 79, 1
Liu, T., Lin, Y.-Q., Hou, S.-J., & Gu, W.-M. 2015, ApJ, 806, 58
Lu, J.-F., Gu, W.-M., & Yuan, F. 1999, ApJ, 523, 340
Matsumoto, R., Kato, S., Fukue, J., & Okazaki, A. T. 1984, PASJ, 36, 71
Mészáros, P. 2001, PThPS, 143, 33
Mitra, S., & Das, S. 2024, ApJ, 971, 28
Narayan, R., Paczynski, B., & Piran, T. 1992, ApJL, 395, L83
Narayan, R., Piran, T., & Kumar, P. 2001, ApJ, 557, 949
Nicuesa Guelbenzu, A., Klose, S., Rossi, A., et al. 2011, A&A, 531, L6
Okuda, T., & Das, S. 2015, MNRAS, 453, 147
Okuda, T., Singh, C. B., Das, S., et al. 2019, PASJ, 71, 49
Paczynski, B. 1991, AcA, 41, 257
Palit, I., Janiuk, A., & Sukova, P. 2019, MNRAS, 487, 755
Peitz, J., & Appl, S. 1997, MNRAS, 286, 681
Popham, R., Woosley, S. E., & Fryer, C. 1999, ApJ, 518, 356
Riffert, H., & Herold, H. 1995, ApJ, 450, 508
Rosswog, S., Ramirez-Ruiz, E., & Davies, M. B. 2003, MNRAS, 345, 1077
Ruffert, M., Janka, H. T., & Schaefer, G. 1996, A&A, 311, 532
Ruffert, M., Janka, H. T., Takahashi, K., & Schaefer, G. 1997, A&A, 319, 122
Ryu, D., Chakrabarti, S. K., & Molteni, D. 1997, ApJ, 474, 378
Sarkar, B., & Das, S. 2016, MNRAS, 461, 190
Sarkar, B., Das, S., & Mandal, S. 2018, MNRAS, 473, 2415
Sen, G., Maity, D., & Das, S. 2022, JCAP, 2022, 048
Singh, M., & Das, S. 2024, Ap&SS, 369, 1
Suková, P., Charzyński, S., & Janiuk, A. 2017, MNRAS, 472, 4327
Wei, Y.-F., & Liu, T. 2022, ApJ, 936, 182
Woosley, S. E. 1993, ApJ, 405, 273
Xue, L., Liu, T., Gu, W.-M., & Lu, J.-F. 2013, ApJS, 207, 23
Yang, R., & Kafatos, M. 1995, A&A, 295, 238
Zalamea, I., & Beloborodov, A. M. 2011, MNRAS, 410, 2302